Dynamics of wrinkling in ultrathin elastic sheets

Finn Box[a], Doireann O'Kiely[a], Ousmane Kodio[a], Maxime Inizan[a], Alfonso A. Castrejón-Pita[b], and Dominic Vella[a,1]

[a]Mathematical Institute, University of Oxford, Oxford OX2 6GG, United Kingdom; and [b]Department of Engineering Science, University of Oxford, Oxford OX1 3PJ, United Kingdom

Edited by Howard A. Stone, Princeton University, Princeton, NJ, and approved August 29, 2019 (received for review April 12, 2019)

The wrinkling of thin elastic objects provides a means of generating regular patterning at small scales in applications ranging from photovoltaics to microfluidic devices. Static wrinkle patterns are known to be governed by an energetic balance between the object's bending stiffness and an effective substrate stiffness, which may originate from a true substrate stiffness or from tension and curvature along the wrinkles. Here, we investigate dynamic wrinkling induced by the impact of a solid sphere onto an ultrathin polymer sheet floating on water. The vertical deflection of the sheet's center induced by impact draws material radially inward, resulting in an azimuthal compression that is relieved by the wrinkling of the entire sheet. We show that this wrinkling is truly dynamic, exhibiting features that are qualitatively different to those seen in quasistatic wrinkling experiments. Moreover, we show that the wrinkles coarsen dynamically because of the inhibiting effect of the fluid inertia. This dynamic coarsening can be understood heuristically as the result of a dynamic stiffness, which dominates the static stiffnesses reported thus far, and allows control of wrinkle wavelength.

dynamic wrinkling | impact | elastocapillarity | fluid–structure interaction

Wrinkling provides a means of reconfiguring slender structures (1, 2) and offers opportunities for characterizing materials through thin sheet metrology (3–5). Control of mechanical properties also permits wrinkle orientation and geometry to be tailored, providing a simple and robust patterning method that can produce periodic structures with regular spacing that ranges from hundreds of nanometers to millimeters (6, 7). This has proved particularly versatile at small scales as an alternative to lithographic techniques: wrinkle formation on soft surfaces has been used to fabricate close-packed nanofluidic channels (8), surfaces with anisotropic wetting properties (9), ordered arrays of self-assembled colloidal particles (10), and optical phase gratings (11, 12).

The formation of wrinkles is induced by compression, with the critical compression and the emergent wavelength of wrinkles depending on a balance between the resistance to bending of the sheet and a stiffness that resists out-of-plane deformation [which may come from a substrate or tension and curvature along the wrinkles (4, 13–15) as well as geometrical confinement (16, 17)]. In applications, the wrinkle wavelength is often controlled by changing the sheet thickness (e.g., through oxidation of thin silica layers (8, 9, 11, 12)]. However, this wavelength is then set once and for all and does not change significantly from its value at onset (18); while the amplitude of wrinkles can be varied by further compression, applications are somewhat limited by this inability to generate different wavelength structures in the same system.

A simple experiment that reveals some of the complexity of wrinkling is the indentation of an ultrathin elastic sheet floating at a liquid to air interface (5, 15, 19–21). Indentation draws material radially inward, in the process creating compressive stresses in the azimuthal direction. At a critical indentation, this compression overcomes the base capillary tension in the sheet (20), and radial wrinkles form (i.e., wrinkles with peaks and valleys that lie along lines of increasing radius). Beyond this wrinkling threshold, the sheet rapidly wrinkles everywhere, but the pattern of wrinkles varies in different regions of the sheet: in a curved central portion, the wrinkle wavelength is controlled by curvature, while beyond this region, the sheet is flat, and the hydrostatic pressure in the liquid instead controls the wrinkle wavelength. In contrast to the case of uniaxial compression discussed above (where the wavelength does not vary with increased confinement), the wrinkles in the central curved portion of a poked sheet become more refined as the confinement is increased by further indentation (15); ultimately, these wrinkles form deep folds (19). In the flat portion, however, the wrinkle wavelength remains constant as indentation progresses. This wavelength, λ_0, is set by the balance between the sheet's bending stiffness, B, and a substrate stiffness K_{sub}, which gives (13, 15)

$$\lambda_0 = 2\pi\left(\frac{B}{K_{\mathrm{sub}}}\right)^{1/4}, \qquad [1]$$

where the substrate stiffness appropriate to a liquid bath is the specific weight of the liquid (i.e., $K_{\mathrm{sub}} = \rho g$ with ρ being the liquid density and g being the acceleration due to gravity). In this article, we investigate how this static picture changes when indentation is performed dynamically via impact.

Dynamic buckling instabilities have been investigated as a route for inducing pattern formation in rigid objects (22, 23) and, also, as a route to understanding plastic crumpling in impacts (24) and brittle fragmentation (25–27). Impact on an elastic sheet has been studied both for a sheet in freefall (27) and a sheet floating on the surface of water (28, 29). In both cases, a longitudinal tensile wave propagates outward from the point of impact at the speed of sound, stretching the sheet, and is followed by a transverse wave that propagates through the stretched

Significance

Elastic instabilities provide a means of generating regular topographies with a well-defined wavelength. For example, a thin elastic film attached to a softer substrate buckles into an array of regular wrinkles under quasistatic compression. The wrinkle wavelength is selected by the mechanical properties of the system so that different wavelengths are typically attained through variation of the film thickness. Here, we show that, for a film of given thickness, variation in the wrinkle wavelength can be achieved dynamically. Our study of impact-induced wrinkling demonstrates that the inertial response of the substrate results in an evolving wrinkle wavelength, opening the route toward dynamic tuning of wrinkle-patterned topographies.

Author contributions: D.V. designed research; F.B., D.O'K., O.K., M.I., A.A.C.-P., and D.V. performed research; F.B. and D.O'K. analyzed data; and F.B., D.O'K., and D.V. wrote the paper.

The authors declare no conflict of interest.

This article is a PNAS Direct Submission.

[1]To whom correspondence may be addressed. Email: dominic.vella@maths.ox.ac.uk.

This article contains supporting information online at www.pnas.org/lookup/suppl/doi:10.1073/pnas.1905755116/-/DCSupplemental.

PHYSICS

domain. A coupling between these 2 waves leads to an azimuthal compression, which gives rise to wrinkling as expected from the static case. In the flat region outside the transverse wave, the wrinkle wavelength is fixed and is explained using the dynamic beam equation, with uniform imposed strain leading to a constant compressive force. Here, we use a similar experimental setup but are able to create wrinkles that evolve dynamically during the course of the experiment, departing from observations in both static indentation experiments and previous dynamic impact experiments.

We investigate dynamic impact on ultrathin polymer sheets subject to an applied background stress (provided by surface tension) (Fig. 1 and Movie S1). The experimental setup is illustrated in Fig. 2*A*. Polystyrene (PS) sheets of thickness $150\,\mathrm{nm} \leq h \leq 530\,\mathrm{nm}$, Young's modulus $E = 3.46\,\mathrm{GPa}$, and Poisson's ratio $\nu = 0.33$ were created by spin coating a PS-in-toluene solution onto glass slides (4). The resulting sheets were cut to have radii $5.5\,\mathrm{mm} \leq R_f \leq 22.7\,\mathrm{mm}$ and floated on water, with surface tension $\gamma_{lv} = 73\,\mathrm{mN\,m^{-1}}$ and density $\rho = 1{,}000\,\mathrm{kg\,m^{-3}}$.* Steel spheres of radii $0.5\,\mathrm{mm} \leq R_s \leq 5.0\,\mathrm{mm}$ and density $\rho_s = 7{,}720\,\mathrm{kg\,m^{-3}}$ were used as impactors, positioned above the center of the sheet in a guiding tube (to ensure that the impact occurred vertically), and released using an electromagnet. The impact and resulting sheet deformation were imaged from below using a high-speed camera. The impact speed $0.6\,\mathrm{m\,s^{-1}} \leq V \leq 2\,\mathrm{m\,s^{-1}}$ was measured by imaging the fall of the sphere from the side. Here, we focus on the deformation of the sheet that occurs at sufficiently early times that the velocity of the sphere is not noticeably affected by impact.†

The images of Fig. 1 show 2 key dynamic features of impact. First, the gross vertical deflection of the sheet (i.e., the shape on which the wrinkles are superimposed) takes the form of a radially propagating transverse wave. This wave is analogous to the ripple observed when a stone is dropped into a pond. Second, wrinkles form in the flat region ahead of the transverse wave, and their wavelength gradually increases—the wrinkles coarsen (Figs. 1 and 2*B*). This is qualitatively different from static indentation experiments (15), which show that wrinkles maintain a constant wavelength with increasing sheet deformation in the flat portion of such a sheet. We note 2 additional departures from static behavior: in static indentation experiments, wrinkles are initially confined to a narrow annulus (5, 20) and reach the edge at indentation depths $\sim 300\,\mu\mathrm{m}$ (21), while folds appear at depths $\sim 600\,\mu\mathrm{m}$–$2\,\mathrm{mm}$ (15, 19). Both of these features appear at impact depths smaller by an order of magnitude ($Vt \sim 100\,\mu\mathrm{m}$) in our dynamic experiments (Fig. 2*B*). In this paper, we will focus on explaining and quantifying wrinkle coarsening in the flat portion of the sheet during impact; to do so, we must first address the transverse wave that drives compression and, hence, wrinkling in the sheet.

Quantitative results for the propagation of the transverse wave are shown in Fig. 3*A*. While the ripples created by dropping a stone into a pond are known to progress according to the inertia to capillary scaling $r_m \propto t^{2/3}$ (29, 30) (black crosses in Fig. 3*A*), we see that, in the presence of an ultrathin elastic sheet, $r_m \propto t^{1/2}$ instead. This scaling is reminiscent of the impact of a sphere into a liquid in the absence of surface tension, for which the contact point between the liquid and solid $r_c = \sqrt{3}(R_s Vt)^{1/2}$ (31, 32). However, the behavior observed here is distinct from this impact phenomenology since, for example, the experimentally measured prefactor in the scaling is dependent on the sheet radius R_f (Fig. 3*A*, *Inset*). To explain this scaling, we consider the behavior at very early times when vertical deflections are small and the effect of gravity on the fluid may be neglected. Since the fluid is initially at rest and the impact is fast (the Reynolds number $\mathrm{Re} = \rho V R_s/\mu \sim 10^3$), we assume that the fluid velocity $\mathbf{u} = \nabla\varphi$ for some velocity potential φ. The speed of sound in both the solid and liquid is $O(10^3)\,\mathrm{m\,s^{-1}}$ so that the timescale for sound waves to traverse the diameter of the sheet is $t_{\mathrm{sound}} = R_f/c \sim 10\,\mu s$. We consider timescales $t \gg t_{\mathrm{sound}}$ so that the fluid is incompressible and

$$\nabla^2\varphi = 0. \quad \textbf{[2]}$$

At the deformed interface $z = w(r,t)$, we impose a kinematic condition,

$$\frac{\partial\varphi}{\partial z} = \frac{\partial w}{\partial t} + \frac{\partial\varphi}{\partial r}\frac{\partial w}{\partial r}, \quad \textbf{[3]}$$

together with a dynamic boundary condition relating the stresses σ_{rr} and $\sigma_{\theta\theta}$ in the sheet to the pressure on the interface $p[r, w(r,t), t]$ via the membrane equation

$$p = -\sigma_{rr}\frac{\partial^2 w}{\partial r^2} - \sigma_{\theta\theta}\frac{1}{r}\frac{\partial w}{\partial r}. \quad \textbf{[4]}$$

The pressure p is, in turn, related to the velocity potential φ through Bernoulli's equation:

$$\rho\left(\frac{\partial\varphi}{\partial t} + \frac{1}{2}|\nabla\varphi|^2\right) + p = 0. \quad \textbf{[5]}$$

In writing Eq. **4**, we have neglected both the bending stiffness and the inertia of the sheet. The PS sheets used in our experiments are very thin and therefore, highly bendable (14, 15, 20); bending stiffness is negligible over the length scale of the transverse wave, although we shall see below that it is important in selecting the wrinkle wavelength.

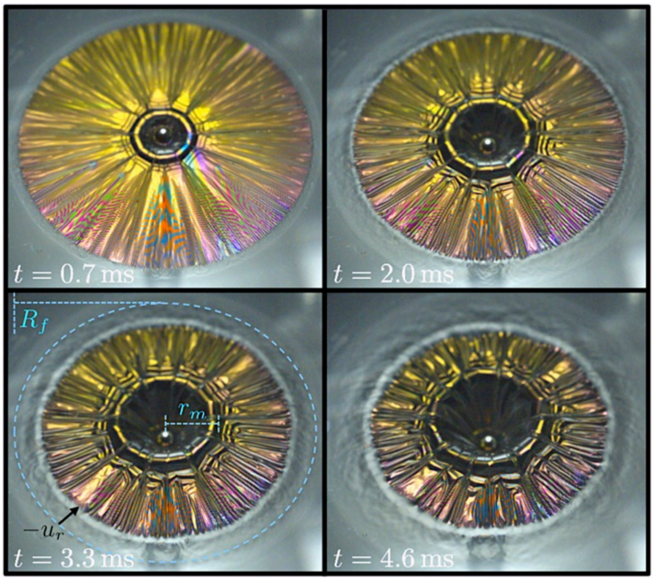

Fig. 1. A steel sphere (radius $R_s = 1.25$ mm) impacts a PS sheet (thickness $h = 350$ nm, radius $R_f = 17.15$ mm, floating at a water to air interface) at speed $V = 0.72\,\mathrm{ms^{-1}}$. Impact draws the outer edge of the sheet inward by a distance $-u_r(R_f, t)$, compressing the sheet even in regions where it remains flat [beyond the propagating transverse wave at $r = r_m(t)$]. The number of radial wrinkles in the sheet decreases with time (i.e., with increasing impact depth Vt), in contrast to the static indentation of a floating sheet (15, 19).

*Note that 1 experiment was performed with a water to glycerol mix with $\gamma_{lv} = 68\,\mathrm{mN\,m^{-1}}$ and $\rho = 1{,}130\,\mathrm{kg\,m^{-3}}$ to test the role of liquid viscosity.

†*Materials and Methods* has details of the experimental procedure, and *SI Appendix* has details of image processing techniques and information about Movies S1 and S2.

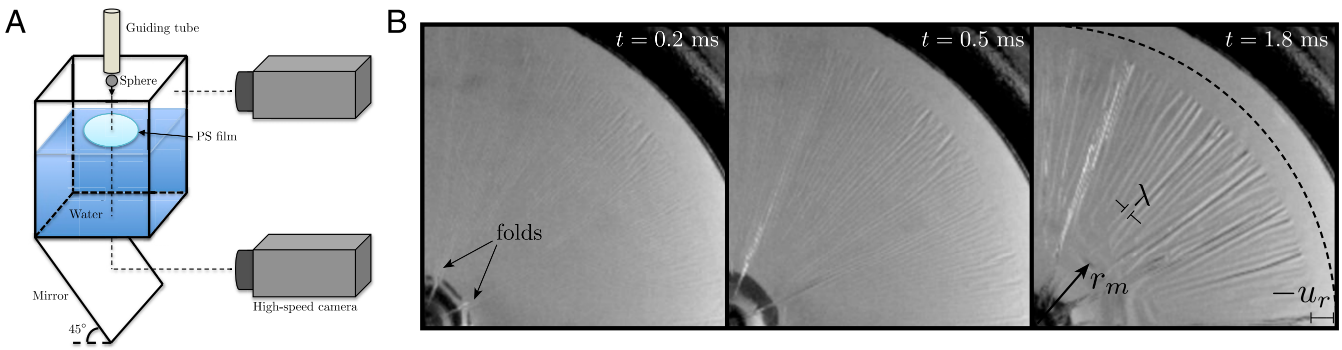

Fig. 2. (*A*) Schematic of the experimental setup used to drop steel spheres onto floating PS sheets. (*B*) Time series of 1 quadrant of a sheet ($h = 450$ nm, $R_f = 17.40$ mm) impacted by a sphere (radius $R_s = 1.75$ mm, $V = 1.17\ \mathrm{ms}^{-1}$) and imaged from below. Note that wrinkles coarsen during the experiment, trebling their mean wavelength in $\sim$1.5 ms. Also highlighted in the images are the onset of folds, the propagation of a transverse wave (visible at radius r_m), and the retraction of the sheet edge (the initial position of which is shown as the dashed circle).

Highly bendable sheets cannot sustain compressive stresses. Instead, wrinkles form very early on, relaxing the compressive hoop stress so that $|\sigma_{\theta\theta}| \ll \sigma_{rr}$. Our experiments focus on times $t \gg t_{\mathrm{sound}}$, for which in-plane stresses are in equilibrium; therefore $\sigma_{rr} \approx \gamma_{lv} R_f / r$ (14, 20) (distinguishing our experiments from many previous studies of dynamic buckling [24–27] and especially ref. 29, where $t \lesssim t_{\mathrm{sound}}$). From a scaling point of view, Laplace's equation (Eq. **2**) suggests that the vertical length scale over which the (infinite) bath of fluid feels the impact $z_* \sim r_m$. The kinematic and dynamic boundary conditions (Eqs. **3**, **4**, and **5**) then suggest that $\varphi_* \sim r_m V \sim \gamma_{lv} R_f V t^2/(\rho r_m^3)$. Combining these scalings, we find that

$$r_m \propto \left(\frac{\gamma_{lv} R_f t^2}{\rho}\right)^{1/4}, \qquad [6]$$

whereas the height of the wave scales with Vt. We emphasize that the predicted scaling $r_m \propto t^{1/2}$ derives from the spatially varying stress $\sigma_{rr} \propto 1/r$ and requires the sheet to be highly wrinkled with the stresses in equilibrium. (By contrast, nonequilibrium stresses generated by a concurrent tensile wave instead cause the transverse wave to propagate as $t^{2/3}$ [29].)

While the impacted sheet might be expected to stretch, in fact $\gamma/(Eh) \sim 10^{-4} \ll 1$ so that the sheets are effectively inextensible. This preserves the length of radial lines (i.e., the radial strain $\epsilon_{rr} \approx 0$) so that the edge retraction follows directly from the vertical deflection: $-u_r(R_f) \approx \frac{1}{2}\int_0^{R_f} (\partial w/\partial r)^2\ \mathrm{d}r \sim (Vt)^2/r_m$. Using Eq. **6**, this yields

$$-u_r(R_f) \propto V^2 \left(\frac{\rho}{\gamma R_f}\right)^{1/4} t^{3/2}. \qquad [7]$$

This scaling prediction is confirmed by experimental data (Fig. 3*B*). We note that our assumption of inextensibility (and hence, the calculation of radial retraction) is only valid because the dominant tension arises from capillarity, which is in contrast to the dynamic indentation experiments of ref. 29 where impact induces significant stretching of the sheet. We also note that, although the power laws predicted by Eqs. **6** and **7** and illustrated in Fig. 3 appear to be robust, there is some spread in the prefactor; we show elsewhere (33) that this spread in prefactor is largely accounted for by the size of the impactor.

The inward displacement of the sheet edge is crucial in driving wrinkling: radial retraction of the sheet $u_r(t)$ leads

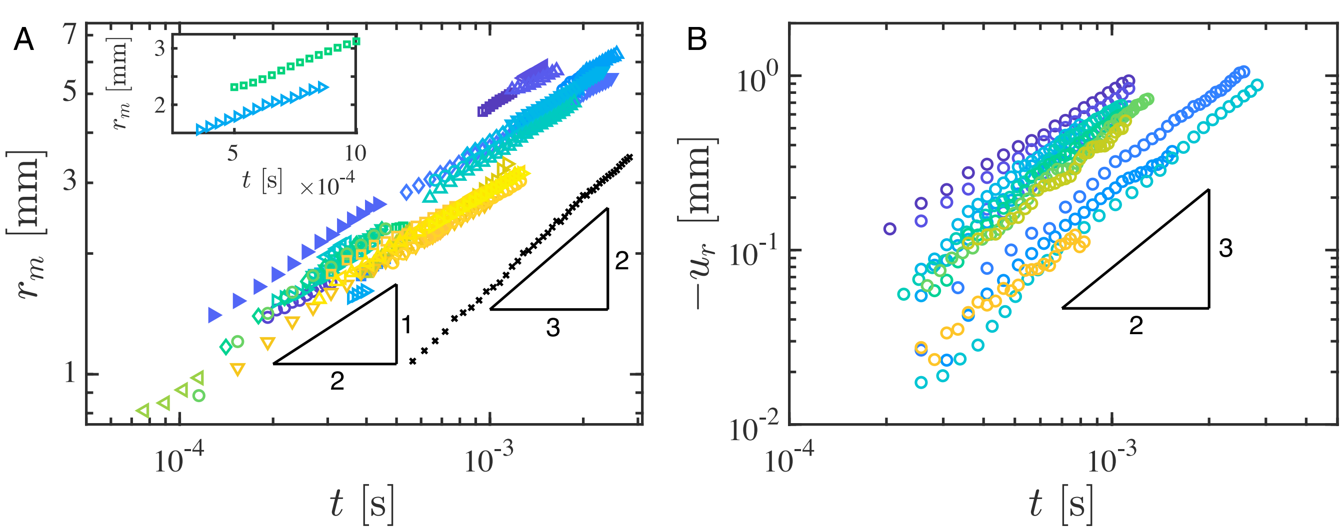

Fig. 3. The propagation of the transverse wave and subsequent retraction of the sheet edge. (*A*) Measurements of the radial position of the capillary wave front on a liquid-to-air interface with no elastic sheet ($\times$) give $r_m \propto t^{2/3}$, different from the behavior with that for an ultrathin PS sheet (colored points). (*Inset*) Wave propagation depends on R_f (=5.51 mm for ▷ and 13.30 mm for ☐). (*B*) The sheet's edge moves radially inward by an amount $-u_r(R_f) \propto t^{3/2}$, corresponding to negligible radial stretching. (Experimental parameters for the data in *A* and *B* are given in *SI Appendix*, Tables S1 and S2, respectively.)

to an azimuthal compression, which is relieved by the growth of wrinkles that accommodate excess material. Experimentally, we observe that the number of wrinkles in a material circle increases approximately linearly with radial distance from the point of impact (Fig. 4*A*) so that the azimuthally averaged wavelength $\bar{\lambda}(t)$ is approximately uniform in the outer region of the sheet at each instant (Fig. 4*A*, *Inset*). This breaks down in the inner region of the sheet, where radial tension and curvature from the transverse wave provide additional stiffnesses (15). The dynamic evolution of $\bar{\lambda}(t)$ in the flat region of the sheet is shown in Fig. 4*B*, and demonstrates that the average wavelength increases (or equivalently, that the number of wrinkles decreases) with time and is smaller than the corresponding static wavelength governed by the fluid's hydrostatic pressure (Eq. **1**).

To understand wrinkle formation and coarsening, we consider a material circle in the flat portion of the sheet ahead of the transverse wave front. We develop a simplified model by considering wrinkling in this material circle driven by the compressive stress arising from radial retraction and moderated by the bending stiffness $B = Eh^3/[12(1-\nu^2)]$ of the sheet and the inertia of the underlying fluid. We only focus on large radial positions so that the curvature of the sheet (associated with the transverse wave) may be neglected and $r \gg \lambda$. We emphasize that the previously neglected bending stiffness of the sheet and small residual compressive hoop stress must both be accounted for over the short length scale associated with wrinkling. We therefore model a freely floating 1-dimensional sheet, which is subject to a compressive force $P(t)$ that mimics the compressive hoop stress $\sigma_{\theta\theta}(t)$ and evolves as a result of an imposed compressive displacement of its ends $\Delta(t)$. The wrinkle coarsening is the result of the sheet being unable to move the liquid instantaneously, but, unlike previous studies (34, 35), here the fluid flow is inertial, not viscous.

We consider a sheet that lies along the x axis and model its out-of-plane displacement, $w(x,t)$, using the beam equation subject to a linearized hydrodynamic pressure from Eq. **5**. A balance between the bending stress, compressive stress, and flow induced by wrinkling gives

$$-\rho\frac{\partial\varphi}{\partial t} = B\frac{\partial^4 w}{\partial x^4} + P(t)\frac{\partial^2 w}{\partial x^2}. \qquad \textbf{[8]}$$

The compressive force $P(t)$ is not known a priori and is determined by imposing a confinement

$$\int_{-\pi r}^{\pi r}\left(\frac{\partial w}{\partial x}\right)^2 \mathrm{d}x = \Delta(t), \qquad \textbf{[9]}$$

which expresses that the sheet wrinkles without changing its length. From a scaling point of view, the kinematic boundary condition gives $\partial\varphi/\partial z \sim \partial w/\partial t$. A scaling analysis of Eq. **8** then gives

$$\lambda \propto \left(\frac{B}{\rho}\right)^{1/5} t^{2/5}, \qquad \textbf{[10]}$$

so that the wavelength is selected simply by a balance between bending stiffness and a "dynamic substrate stiffness" (see below) associated with fluid inertia. The scaling Eq. **10** gives a reasonable account of our experimental data (Fig. 4*B*). We note that the radial position r and confinement $\Delta(t)$ affect the wrinkle amplitude through Eq. **9** but not the scaling argument Eq. **10**, which is derived from Eq. **8** only. Furthermore, the length constraint Eq. **9** prevents the existence of an exact similarity solution of the form Eq. **10**; numerical solutions presented in ref. 33 demonstrate that the scaling of Eq. **10** may have a logarithmic-type correction.

We have studied the dynamic wrinkling of an ultrathin elastic sheet floating on a liquid interface, highlighting several key features of this motion. The motion $r_m \propto t^{1/2}$ of the transverse wave illustrates the large change in the state of stress caused by highly developed wrinkling, while the evolution of the wrinkle pattern is very different to that observed statically (15, 20): fluid inertia

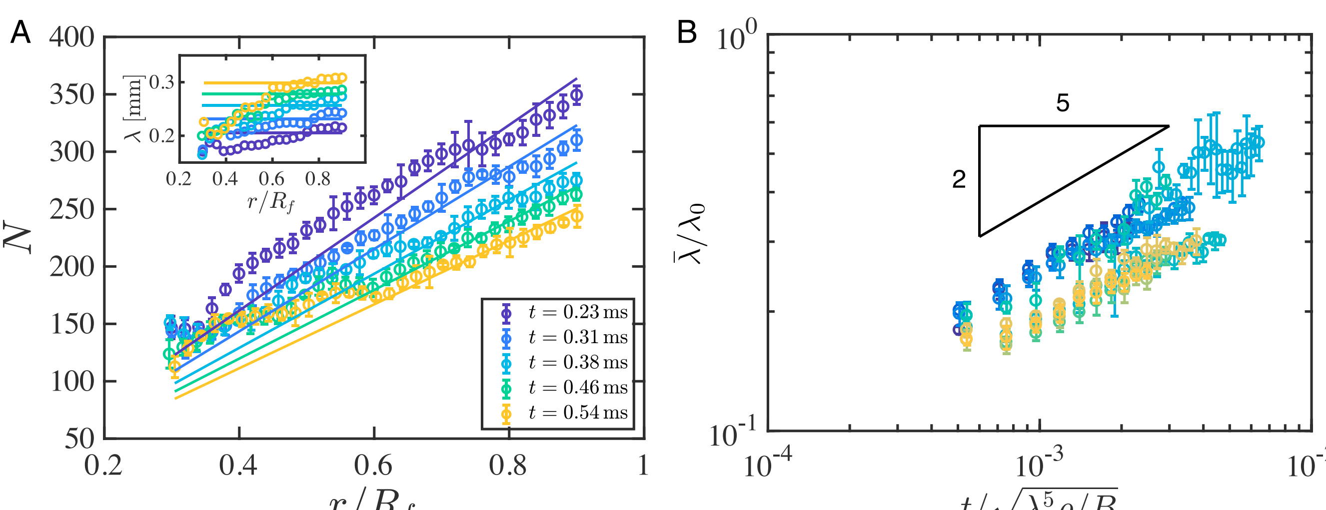

Fig. 4. The instantaneous and dynamically evolving wrinkle wavelengths. (*A*) The number of wrinkles N increases approximately linearly with radial distance from the point of impact, corresponding to an instantaneous average wavelength that is approximately uniform (*Inset*). Data points show measurements at different times as indicated in the legend; solid lines indicate linearity and a fixed value (*Inset*). Here, $h = 450$ nm, $R_f = 13.3$ mm, $R_s = 1.25$ mm, and $V = 1.11\,\mathrm{m\,s^{-1}}$. (*B*) The mean wavelength $\bar{\lambda}$ of the radial wrinkles in a fixed material circle, $r(t) = 0.8[R_f - u_r(R_f, t)]$, increases with time. $\bar{\lambda}$ was measured by counting the number of wrinkles and averaging azimuthally; $\bar{\lambda}$ is normalized with the static wavelength λ_0 given by Eq. **1**. Experimental parameters for B are given in *SI Appendix*, Table S3. In *B*, the scaling of Eq. **10** is highlighted by the triangle. The error bars represent the SD of measurements obtained in 10 intensity signals from neighboring pixel strips of an unwrapped image (*A*) or spatiotemporal plot (*B*); *SI Appendix* has additional details. Here, the axes are scaled with the static wavelength $\lambda_0 \approx 1.5{-}1.7$ mm and the corresponding timescale $(\lambda_0^5\rho/B)^{1/2} \approx 0.7$ s.

slows out-of-plane deformation of the sheet, selecting a dynamically evolving but almost spatially uniform wrinkle wavelength. Moreover, the effect of the fluid inertia can be understood as the result of a dynamic substrate stiffness, $K_{\rm dyn}$, which supplements the substrate-, tension-, and curvature-induced stiffnesses that have been introduced for static wrinkle patterns (13–15). In particular, Eq. **10** can be rewritten as $\lambda \propto (B/K_{\rm dyn})^{1/4}$, with $K_{\rm dyn} \sim \rho \times \lambda / t^2$ arising from the hydrodynamic pressure associated with accelerating liquid to accommodate increasing λ: by addressing a dynamic scenario, we effectively introduce a source of stiffness that competes with the bending stiffness of the sheet to control the wrinkle wavelength. We note that, at sufficiently late times, this additional hydrodynamic pressure will decrease below the typical hydrostatic pressure, ultimately leading to quasistatic wrinkles governed by the usual static stiffness $K_0 = \rho g$.

A surprising feature of our main results (Eqs. **6** and **10**) is that they do not have explicit dependencies on the impact velocity V. This is because V affects the magnitude of the vertical displacement of the sheet but not how fast this disturbance propagates: that speed is instead set by the intrinsic properties of the sheet and liquid. Note, however, that the radial displacement at the edge of the film (Eq. **7**) does depend on V, since it is induced by the vertical motion. Nevertheless, the wrinkle wavelength λ is independent of V, since the amount of compression to be accommodated merely changes the amplitude of wrinkles.

We expect the dynamic picture that we have presented here to hold while the transverse wave is traveling across the sheet (i.e., while $r_m \ll R_f$), which, in turn, requires $t \ll (\rho R_f^3/\gamma)^{1/2}$. At the same time, we also need to ensure that the dynamic wrinkle wavelength $\lambda \ll \lambda_0 = (B/\rho g)^{1/4}$, which amounts to the requirement that $t \ll (\lambda_0/g)^{1/2}$ (note that the data in Fig. 4*B* all readily satisfy this constraint). Both of these results are independent of the velocity of the impactor, V. The key point that determines whether an impact is inertial in the sense considered here is whether the vertical distance traveled during this early time is large compared with the critical vertical displacement at which wrinkling occurs in the static problem, $\delta_c \sim \gamma/(Eh\rho g)^{1/2}$ (20, 21). This comparison gives us that the wrinkling of the sheet is governed by the inertia of the fluid if

$$V \gg V_c = \left(\frac{\gamma^2}{Eh\cdot\rho}\right)^{1/2} \max\left[\left(\frac{\gamma}{R_f^3 \rho g}\right)^{1/2}, \lambda_0^{-1/2}\right]; \qquad [11]$$

for the parameters typical of the floating PS sheets considered in our experiments, $V_c = O(1\ \mathrm{mm\,s^{-1}})$ so that the impacts that we consider, with $V = O(1\ \mathrm{m\,s^{-1}})$, all lie well within this regime.

Our experiments suggest that a dynamic substrate stiffness may provide a means of breaking away from the single static wavelength that is selected by material properties alone, allowing the wavelength to be altered without resorting to nonuniform substrates or coatings (36). This is a route for tunable wrinkle formation that may prove to be a useful fabrication technique in a range of engineering applications that require regular patterned topographies (6, 37). In particular, we have shown that this wavelength change can occur very quickly, with a doubling of the mean wavelength in around 1 ms (Figs. 2*B* and 4*B*).

The rapid coarsening of wrinkle wavelength that we have presented occurs with wavelengths on the order of $100\ \mu\mathrm{m}$, making it readily observable. However, the underlying mechanism is scale independent, provided that the Reynolds number of the fluid flow remains sufficiently large that inertia dominates viscosity. This mechanism might, therefore, be suitable for reproduction at similar scales but with still thinner sheets to obtain wrinkles at smaller length scales. A key objective would be to produce wrinkle wavelengths small enough for use in applications with visible light. For example, wrinkle wavelengths around $\lambda \approx 4.7\ \mu\mathrm{m}$ were used in ref. 38 to focus light; our model suggests that extremely thin ($h \sim 7$ nm) PS sheets (39) would generate wrinkles with similar wavelengths over a fraction of a millisecond. Many optical applications, including photonic materials (40) and Bragg gratings (41), require periodic structures with period comparable with the wavelength of visible light. If our impact protocol was implemented with monolayer graphene floating on water [with bending rigidity $B \sim 10^{-19}$ J (42)], our theory predicts that the wrinkle wavelength would double from $\lambda \approx 400$ nm to $\lambda \approx 800$ nm (thereby transitioning from the wavelength of blue light to beyond that of red light) on a timescale of $\sim 2\ \mu\mathrm{s}$.

Applications of dynamic wrinkling would benefit from other means of generating the rapid azimuthal compression required for wrinkling. While high-speed indentation with a linear actuator could replace impact, the negative thermal expansion coefficient of graphene (43) could also be exploited; indeed, contraction caused by ultrafast optical excitation can create a compressive strain of magnitude 6×10^{-4} within 100 ps (44). This compressive strain would be sufficient to overcome the isotropic tension caused by surface tension, $\gamma/(Eh) \approx 2 \times 10^{-4}$, and it could, therefore, be used to induce dynamic wrinkling. The practicalities of achieving such rapid wrinkling in ultrathin sheets deserve further investigation.

Materials and Methods

Materials. PS sheets were created by dissolving PS powder (Goodfellow) in toluene (anhydrous, 99.8%; Sigma-Aldrich) and spin coating the solution onto glass slides (4) at 1,000 rpm for 60 s (spin coater Polos SPIN150i). Films of different thicknesses, in the range 150 nm $\le h \le$ 530 nm, were created by varying the concentration of the solution (from 2 to 4.5 g PS per 100 mL toluene), and they were measured using a thin-film analyzer (F20; Film Metrics). The resulting sheets were cut into circular disks using a diamond-tipped cutting tool and floated on water, with reported surface tension $\gamma_{lv} \approx 73\ \mathrm{mN\,m^{-1}}$, viscosity $\mu \approx 0.89$ mPa s, and density $\rho \approx 1{,}000\ \mathrm{kg\,m^{-3}}$. The resulting sheet radius was measured from images and was varied in the range 5.5 mm $\le R_f \le$ 22.7 mm.

Methods. Impact experiments were performed by dropping steel spheres (Simply Bearings; radii 0.5 mm $\le R_s \le$ 5.0 mm and density $\rho_s =$ 7,720 $\mathrm{kg\,m^{-3}}$) onto floating PS films. A schematic of the experimental setup is shown in Fig. 2, with a video provided as Movie S1. Spheres were released using a custom-built electromagnet positioned so that spheres impacted the center of the sheet. A guiding tube was used to ensure that the impact occurred vertically. The impact was imaged from below using a high-speed video camera (Miro 310; Phantom), typically at a frame rate of 39, 024 Hz with 256 $\times$ 256 pixels and with a spatial resolution of 0.02 mm per pixel. The impact speed 0.6 $\mathrm{m\,s^{-1}} \lesssim V \le 2\ \mathrm{m\,s^{-1}}$ was measured by imaging the fall of the sphere at 1,000 Hz using a second camera (FinePix HS10; Fujifilm).

The results presented correspond to approximately constant impact velocities, with data only shown up to the time at which the predicted contact radius becomes comparable with the sphere radius (33). The only exception to this is in Fig. 3*A*, *Inset*, where we have displayed data over a longer time interval to clearly illustrate the dependence on R_f.

We performed 1 impact experiment in which the underlying fluid had a higher viscosity than water to assess the influence of liquid viscosity. The liquid was a glycerol to water mixture (55:45% by volume) with measured dynamic viscosity $\mu = 13$ mPa s, surface tension coefficient $\gamma_{lv} = 68\ \mathrm{mN\ m^{-1}}$, and density $\rho = 1{,}130\ \mathrm{kg\ m^{-3}}$. The transverse wave front data for this experiment are illustrated in Fig. 3*A* and highlighted with filled-in markers. The results are consistent both with the other experiments and with the theoretical prediction, confirming that viscosity does not play a significant role and validating our neglect of fluid viscosity.

The measured values of the instantaneous wavelength were distributed around some mean value rather than being a single well-defined wavelength (*SI Appendix*); the average wavelength reported herein was determined by counting visible wrinkles in images and averaging this number over the length of a particular material circle. We investigate the distribution of wavelengths in more detail in another paper (33).

ACKNOWLEDGMENTS. The research leading to these results received funding from the Royal Society (A.A.C.-P.), the European Research Council (ERC) under European Union's Horizon 2020 Program/ERC Grant 637334 (D.V.), and the Oxford University Press John Fell Fund (F.B.).

1. Y. W. Wong, S. Pellegrino, Wrinkled membranes. Part I. Experiments. *J. Mech. Mater. Struct.* **1**, 3–25 (2006).
2. P. M. Reis, A perspective on the revival of structural (in)stability with novel opportunities for function: From buckliphobia to buckliphilia. *J. Appl. Mech.* **82**, 111001 (2015).
3. C. M. Stafford *et al.*, A buckling-based metrology for measuring the elastic moduli of polymeric thin films. *Nat. Mater.* **3**, 545–550 (2004).
4. J. Huang *et al.*, Capillary wrinkling of floating thin polymer films. *Science* **317**, 650–653 (2007).
5. M. M. Ripp, V. Fery, T. Zhang, J. D. Paulsen, Geometry underlies the mechanical stiffening and softening of thin sheets. https://arxiv.org/abs/1804.02421 (6 April 2018).
6. M. M. Schweikart, A. Fery, Controlled wrinkling as a novel method for the fabrication of patterned surfaces. *Microchim. Acta* **165**, 249–263 (2009).
7. F. A. Bayley, J. L. Liao, P. N. Stavrinou, A. Chiche, J. T. Cabral, Wavefront kinetics of plasma oxidation of polydimethylsiloxane: Limits for sub-mm wrinkling. *Soft Matter* **10**, 1155–1166 (2014).
8. S. Chung, J. H. Lee, M. W. Moon, J. Han, R. Kamm, Non-lithographic wrinkle nanochannels for protein preconcentration. *Adv. Mater.* **20**, 3011–3016 (2008).
9. J. Y. Chung, J. P. Youngblood, C. M. Stafford, Anisotropic wetting on tunable micro-wrinkled surfaces. *Soft Matter* **3**, 1163–1169 (2007).
10. C. H. Lu, H. Mohwald, A. Fery, A lithography-free method for directed colloidal crystal assembly based on wrinkling. *Soft Matter* **3**, 1530 (2007).
11. N. Bowden, W. T. S. Huck, K. E. Paul, G. M. Whitesides, The controlled formation of ordered, sinusoidal structures by plasma oxidation of an elastomeric polymer. *Appl. Phys. Lett.* **75**, 2557–2559 (1999).
12. C. Harrison, C. M. Stafford, W. Zhang, A. Karim, Sinusoidal phase grating created by a tunably buckled surface. *Appl. Phys. Lett.* **85**, 4016–4018 (2004).
13. E. Cerda, L. Mahadevan, Geometry and physics of wrinkling. *Phys. Rev. Lett.* **90**, 074302 (2003).
14. B. Davidovitch, R. D. Schroll, D. Vella, M. Adda-Bedia, E. Cerda, Prototypical model for tensional wrinkling in thin sheets. *Proc. Natl. Acad. Sci. U.S.A.* **108**, 18227–18232 (2011).
15. J. D. Paulsen *et al.*, Curvature-induced stiffness and the spatial variation of wavelength in wrinkled sheets. *Proc. Natl. Acad. Sci. U.S.A.* **113**, 1144–1149 (2016).
16. B. Davidovitch, Y. Sun, G. M. Grason, Geometrically incompatible confinement of solids. *Proc. Natl. Acad. Sci. U.S.A.* **116**, 1483–1488 (2019).
17. L. Stein-Montalvo, P. Costa, M. Pezzulla, D. P. Holmes, Buckling of geometrically confined shells. *Soft Matter* **15**, 1215–1222 (2019).
18. S. Cai, D. Breid, A. J. Crosby, Z. Suo, J. W. Hutchinson, Periodic patterns and energy states of buckled films on compliant substrates. *J. Mech. Phys. Solids* **59**, 1094–1114 (2011).
19. D. P. Holmes, A. J. Crosby, Draping films: A wrinkle to fold transition. *Phys. Rev. Lett.* **105**, 038303 (2010).
20. D. Vella, J. Huang, N. Menon, T. P. Russell, B. Davidovitch, Indentation of ultrathin elastic films and the emergence of asymptotic isometry. *Phys. Rev. Lett.* **114**, 014301 (2015).
21. D. Vella, B. Davidovitch, Regimes of wrinkling in an indented floated sheet. *Phys. Rev. E* **98**, 013003 (2018).
22. H. Vandeparre *et al.*, Hierarchical wrinkling patterns. *Soft Matter* **6**, 5751–5756 (2010).
23. F. Box, R. Bowman, T. Mullin, Dynamic compression of elastic and plastic cellular solids. *App. Phys. Lett.* **103**, 151909 (2013).
24. D. Karagiozova, M. Alves, Dynamic elastic-plastic buckling of structural elements: A review. *Appl. Mech. Rev.* **61**, 040803 (2008).
25. J. R. Gladden, N. Z. Handzy, A. Belmonte, E. Villermaux, Dynamic buckling and fragmentation in brittle rods. *Phys. Rev. Lett.* **94**, 035503 (2005).
26. R. Vermorel, N. Vandenberghe, E. Villermaux, Rubber band recoil. *Proc. Roy. Soc. A* **463**, 641–658 (2007).
27. R. Vermorel, N. Vandenberghe, E. Villermaux, Impact on thin elastic sheets. *Proc. Roy. Soc. A* **465**, 823–842 (2009).
28. L. Duchemin, N. Vandenberghe, Impact dynamics for a floating elastic membrane. *J. Fluid Mech.* **756**, 544–554 (2014).
29. N. Vandenberghe, L. Duchemin, Impact on floating membrane. *Phys. Rev. E.* **93**, 052801 (2016).
30. J. B. Keller, M. J. Miksis, Surface tension driven flows. *SIAM J. Appl. Math.* **43**, 268–277 (1983).
31. H. Wagner, Über stoß- und gleitvorgänge an der oberfläche von flüssigkeiten (phenom- ena associated with impacts and sliding on liquid surfaces). *Zeit. Angew. Math. Mech.* **12**, 193–215 (1932).
32. J. Philippi, P.-Y. Lagrée, A. Antkowiak, Drop impact on a solid surface: Short-time self-similarity. *J. Fluid Mech.* **795**, 96–135 (2016).
33. D. O'Kiely, F. Box, O. Kodio, J. P. Whiteley, D. Vella, Impact on a floating elastic sheet: Ripple propagation and wrinkle coarsening. https://arxiv.org/abs/1811.11288 (14 November 2018).
34. O. Kodio, I. M. Griffiths, D. Vella, Lubricated wrinkles: Imposed constraints affect the dynamics of wrinkle coarsening. *Phys. Rev. Fluids* **2**, 014202 (2017).
35. J. Chopin, M. Dasgupta, A. Kudrolli, Dynamic wrinkling and strengthening of an elastic filament in a viscous fluid. *Phys. Rev. Lett.* **119**, 088001 (2017).
36. J. Schleifer, J. Marthelot, T. J. Jones, P.-T. Brun, The fingerprint of a flow: Wrinkle patterns in nonuniform coatings on pre-stretched soft foundations. *Soft Matter* **15**, 1405–1412 (2019).
37. S. Yang, K. Khare, P.-C. Lin, Harnessing surface wrinkle patterns in soft matter. *Adv. Func. Mater.* **20**, 2550–2564 (2010).
38. R. Li *et al.*, Generation of diffraction-free optical beams using wrinkled membranes. *Sci. Rep.* **3**, 2775 (2013).
39. J. Chang, K. B. Toga, J. D. Paulsen, N. Menon, T. P. Russell, Thickness dependence of the young's modulus of polymer thin films. *Macromolecules* **51**, 6764–6770 (2018).
40. H. Fudouzi, Y. Xia, Photonic papers and inks: Color writing with colorless materials. *Adv. Mater.* **15**, 892–896 (2003).
41. Z. Shen, L. Wu, S. Zhu, Y. Zheng, X. Chen, Random lasing action in a poly-dimethylsiloxane wrinkle induced disordered structure. *Appl. Phys. Lett.* **105**, 021106 (2014).
42. Q. Lu, M. Arroyo, R. Huang, Elastic bending modulus of monolayer graphene. *J. Phys. D Appl. Phys.* **42**, 102002 (2009).
43. D. Yoon, Y.-W. Son, H. Cheong, Negative thermal expansion coefficient of graphene measured by Raman spectroscopy. *Nano Lett.* **11**, 3227–3231 (2011).
44. J. Hu, G. M. Vanacore, A. Cepellotti, N. Marzari, A. H. Zewail, Rippling ultrafast dynamics of suspended 2d monolayers, graphene. *Proc. Natl Acad. Sci. U.S.A.* **113**, E6555–E6561 (2016).